JCI insight

Magnetic resonance imaging of cerebrospinal fluid outflow after low-rate lateral ventricle infusion in mice

Yann Decker, … , Klaus Fassbender, Steven T. Proulx

JCI Insight. 2021. https://doi.org/10.1172/jci.insight.150881.

Resource and Technical Advance | In-Press Preview | Neuroscience | Vascular biology

Graphical abstract

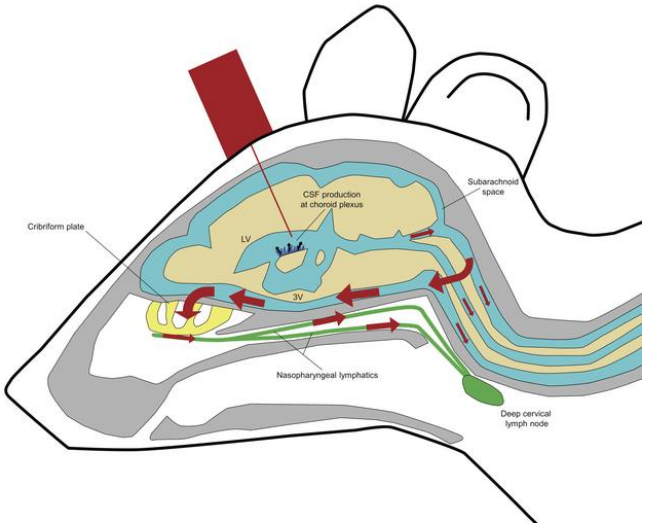

Magnetic resonance imaging of cerebrospinal fluid outflow after low-rate lateral ventricle infusion in mice

Yann Decker[1], Jonas Krämer[1], Li Xin[2], Andreas Müller[3], Anja Scheller[4], Klaus Fassbender[1], Steven T. Proulx[2]

[1]Department of Neurology, Saarland University Medical Center, Homburg, Germany
[2]Theodor Kocher Institute, University of Bern, Bern, Switzerland
[3] Clinic for Diagnostic and Interventional Radiology, University of the Saarland, Homburg, Germany
[4] Molecular Physiology, Center for Integrative Physiology and Molecular Medicine (CIPMM), University of Saarland, Homburg, Germany

The authors have declared that no conflict of interest exists.

Corresponding authors:

Yann Decker, PhD
Department of Neurology
Saarland University Medical Center
66421 Homburg/Saar, Germany
Tel.: ++49-6841-1624215
Email: yann.decker@uks.eu

Steven T. Proulx, PhD
Theodor Kocher Institute
University of Bern
CH-3012 Bern, Switzerland
Tel.: ++41-31-631-5390
Email: steven.proulx@tki.unibe.ch

Abstract

The anatomical routes for the clearance of cerebrospinal fluid (CSF) remain incompletely understood. However, recent evidence has given strong support for routes leading to lymphatic vessels. A current debate centers upon the routes through which CSF can access lymphatics, with evidence emerging for either direct routes to meningeal lymphatics or along cranial nerves to reach lymphatics outside the skull. Here, a method was established to infuse contrast agent into the ventricles using indwelling cannulae during imaging of mice at 2 and 12 months of age by magnetic resonance imaging. As expected, a significant decline in overall CSF turnover was found with aging. Quantifications demonstrated that the bulk of the contrast agent flowed from the ventricles to the subarachnoid space in the basal cisterns. Comparatively little contrast agent signal was found at the dorsal aspect of the skull. The imaging dynamics from the two cohorts revealed that the contrast agent cleared from the cranium through the cribriform plate to the nasopharyngeal lymphatics. On decalcified sections, we confirmed that fluorescently-labeled ovalbumin drains through the cribriform plate and can be found within lymphatics surrounding the nasopharynx. In conclusion, routes leading to nasopharyngeal lymphatics appear to be a major efflux pathway for cranial CSF.

Keywords:

Cerebrospinal fluid, lymphatic vessel, contrast enhanced-magnetic resonance imaging, clearance, aging

Introduction

Cerebrospinal fluid (CSF) is produced within the ventricles by the choroid plexuses and circulates within the subarachnoid spaces around the brain and spinal cord. Historically, it was concluded that CSF would leave the central nervous system (CNS) via direct pathways through outcroppings of arachnoid tissue into the venous sinuses of the dura mater (1, 2). However, in recent decades it has become commonly accepted that lymphatic vessels play a significant role in the process of CSF drainage (3-6). Recent studies in rodents have demonstrated that lymphatic vessels appear to be the exclusive clearance route for tracers injected into the CSF, even for small molecular weight solutes (7, 8). An active area of research has focused upon the anatomical routes of outflow that CSF takes to access the lymphatic vessels. Support exists for access of CSF to lymphatic vessels that have been recently rediscovered in the dura mater (9-11) and for efflux along cranial or spinal nerves to reach extracranial lymphatics (7, 12-15). Of the perineural routes, evidence in many different species exists for routes along olfactory nerves through the cribriform plate (5, 10, 16-20).

Imaging techniques have long been utilized to assess CSF outflow of tracers (6). Traditionally, these techniques have employed X-ray or scintigraphic measurements (21, 22). Recently, two-photon or near-infrared fluorescence techniques (7-9, 13, 14, 23) have been developed to allow sensitive in vivo readouts within the CNS (imaging through-skull or through-spine), to specific efflux pathways (imaging through vomeronasal bones into the nasal region or imaging of lymphatic vessels draining to the superficial cervical or mandibular lymph nodes) or as a readout for transport to blood from multiple pathways. However, these methods can only allow assessments at one particular region at a relatively superficial level. On the other hand, contrast enhanced-magnetic resonance imaging (CE-MRI) techniques have the advantage of 3D imaging of the entire cranial or spinal regions in the context of the surrounding soft-tissue anatomy, with sufficient temporal resolution to track the dynamics of contrast agent outflow, and have a more immediate translational potential to the clinic (8, 11-13, 15, 24).

One valid criticism of tracer injection studies is that they may inherently introduce artifacts due to relatively large acute volumes introduced into the CSF. In the mouse, with an estimated CSF volume of 35 μL (2), injections of 5 to 10 μL made within a short period likely introduce elevated pressure conditions that will affect the dynamics and routes of outflow (8, 25). Our group has attempted to address this issue by establishment of an indwelling cannula into the lateral ventricle of mice that allows slow infusion during imaging acquisition (13) at rates below the published rates for CSF production (2, 26). We have utilized this cannula system to allow MRI measurements of spinal CSF distribution and sacral outflow during the infusion of contrast agent (13). Similar cisterna magna infusion setups have also recently been employed by other groups to examine cranial CSF distribution (12, 15).

Alterations in CSF circulation may have significant effects on the pathogenesis of neurological conditions associated with the aging process, including dementia and stroke. Many research groups have now demonstrated that a slower overall efflux of CSF occurs during the aging process (7, 11, 14). Thus, we have utilized this expected difference in CSF turnover dynamics between younger (2-3 month old) and older (12 month old) mice to aid in validation of MRI quantifications. Second, we have investigated potential efflux routes by analyzing the contrast agent signal dynamics at several different locations within the CNS and the draining cranial lymph nodes. We hypothesized that differences in signal dynamics quantified between the two age groups will be apparent only at the major site(s) of efflux.

Results

Tracer infused into the lateral ventricle follows a continuous outflow route from the nasal cavity to the draining cervical lymph nodes

Since CSF is principally produced by the choroid plexuses that are located in the ventricles, we decided to analyze the flow of tracer following an intraventricular low-rate infusion of a 17 kDa dendritic gadolinium-based contrast agent, Gadospin D (Fig. 1a). We chose Gadospin D rather than a low molecular weight contrast agent to limit potential diffusion into the brain parenchyma from the ventricular injection site. After stereotactic implantation of an indwelling cannula in the right lateral ventricle, mice were positioned in a prone position on a horizontal MRI platform. A polyethylene line filled with contrast agent was subsequently connected at one end to the cannula and at the other end to an infusion pump. After a baseline pre-contrast scan, an infusion of the contrast agent was started at a rate of 0.1 μl/min for 60 min and a series of CE-MRI images were collected over the course of 90 min. This experimental setup allowed us acquire images of the animal throughout the course of the infusion of a macromolecular contrast agent at rates not excessive to physiological levels.

We first determined the general pattern of the spread of Gadospin D by generating maximum intensity projection images at each timepoint to allow a 3D dynamic visualization of the contrast agent (Video 1). An initial filling of the ventricular system was apparent with spreading ventrally to the basal cisterns and under the olfactory bulbs within the first 15 min after the start of the infusion. With increasing time, it was observable that the signal intensity of the tracers was progressively detectable in the nasal cavity, in the nasopharyngeal region and in the deep and superficial lymph nodes (Fig. 1b). Moreover, as observable in Fig. 1c and Video 1, it was possible to identify a continuous anatomic route along the nasopharynx that emerged from the nasal cavity and connected to the deep cervical lymph nodes. Connections also were apparent from the deep cervical lymphatics to the superficial cervical (or mandibular) lymph nodes, as previously shown using near-infrared imaging (7).

Reduced tracer clearance from the ventricles and slower efflux to draining lymph nodes in older mice

It has recently been demonstrated that CSF production and drainage are both reduced in aged mice suggesting that the overall CSF turnover is slower with aging (7, 14, 27). During and immediately after the low-rate intraventricular infusion, we investigated the clearance of Gadospin D from the ventricular system in two groups of mice of either 2-3 months (n=7) or 12 months of age (n=6). While the low rate infusion of contrast agent took place during the first 60 min, we observed that the signal intensity in the contralateral ventricles reached a peak at around 40 min and then progressively decreased in both age groups (Fig. 2a; Supp Fig.1a). At later timepoints, we could observe significantly stronger decreased signal intensity in the contralateral ventricle of the group of younger mice. As no significant difference was observed in the volume of the contralateral ventricles (Fig. 2b) between the two groups, we concluded that a decrease in the rate of CSF turnover is responsible for the reduced contrast agent clearance observed in the 12 month old mice.

Our previous studies have shown that lymphatic outflow from CSF is reduced in 18 month old mice compared to 2 month old mice following a bolus injection of a macromolecular fluorescently-labeled tracer (7). We tested whether this difference would be apparent by MRI in mice of 12 months of age by quantifying the signal intensity of the contrast agent in regions-of-interest (ROIs) positioned in the deep and superficial cervical lymph nodes. Dynamic CE-MRI quantification revealed less contrast agent signal in both groups of cervical lymph nodes in the 12 month old mice compared to the group of younger mice (Fig. 2c,d; Supp Fig.1b,c). Quantifications of the volume of 3D reconstructions of the cervical lymph nodes also did not show significant differences between the two age groups (Supp Fig.1d,e).

In sum, we observed that with aging, a low-rate infusion of a macromolecular contrast agent is associated with reduced clearance from the ventricles and a delayed transport to draining lymph nodes which is consistent with previous studies by our group and others. Thus, we next aimed to exploit these differences in CSF turnover dynamics between the two age groups of mice to help identify the major efflux routes from the ventricular system to the lymphatic system.

Contrast agent flows along the ventral aspect of the brain and down the spine

CSF has recently been proposed to reach the dura mater on the dorsal aspect of the skull where it is hypothesized to be either directly or indirectly drained by meningeal lymphatic vessels leading to the deep cervical lymph nodes (9, 28-30). Previous work has highlighted lymphatic vessels in the dural tissue surrounding the sagittal and the transverse sinuses to be “hotspots” for uptake from the CSF. Thus, following intraventricular infusion of Gadospin D, we quantified the signal intensity in two ROIs of the dorsal aspect of the skull in proximity to these regions. In both areas, we could

observe only a limited maximum change in signal intensity compared to baseline (sagittal sinus ROI: <42%; quadrigeminal cistern ROI: < 120%) and no significant differences at any timepoint between the groups of 2 month and 12 month old mice (Fig 3 a,b,c; Supp Fig.2 a,b).

On the other hand, quantifications of ROIs in the ventral region (at the basal cisterns around the circle of Willis and the internal carotid artery) show a substantial increase in maximum change in signal intensity compared to baseline (CoW ROI: >700%; Internal carotid ROI: >700%) suggesting that this area is the major site of contrast agent bulk flow (Fig 3 a,d,e; Supp Fig.2 c,d). Moreover, in the two regions investigated the signal intensity was significantly quantitatively higher at earlier time points in young mice compared to the group of 12 month old mice. These results indicate that an infused macromolecular tracer principally flows with the CSF through the ventral, rather than dorsal, aspect of the skull.

As CSF leaving the ventricles has free communication with the subarachnoid space around the spinal cord, we also quantified the dynamics in the ventral aspect of the cervical spine (Supp Fig.3a). We observed a rapid increase in signal intensity in the group of young mice that reached a maximum percentage change of more than 600%. Conversely, in the group of 12 month old mice, the signal intensity increase was delayed and only reached approximately half ot the value observed in young mice. Thus, CSF tracer flow from the ventricular system to the spine can be easily demonstrated with CE-MRI and exhibits the expected decline with aging.

Recent work has introduced the concept of glymphatic flow that would theoretically aid in CSF/solute penetration into the brain parenchyma along paraarterial spaces. Recent MRI studies have shown that low molecular weight contrast agents, such as gadoteric acid (Gd-DOTA), do indeed demonstrate signal enhancement within the parenchyma (31-36). However, we were unable to confirm a significant influx of the Gadospin D contrast agent (17 kDa) into the brain cortex in either group (maximum percentage change of 17%). This limited signal enhancement of a macromolecular contrast agent within the brain is consistent with our earlier study (8) and others (12).

Thus, we conclude from this study that bulk flow routes to the basal cisterns and the subarachnoid space of the spinal canal are the major pathways for CSF macromolecular distribution from the ventricular system.

Dynamics of CSF contrast agent outflow support route(s) leading to the nasopharyngeal lymphatics

After observing that a significant portion of the tracer reaches the basal cisterns, we aimed to elucidate the potential anatomical pathways from this location that might be used to reach the cervical draining lymph nodes. Based on our observation that the bulk of the contrast agent appeared to flow continuously from the region of the olfactory bulbs to the

nasopharynx and to the draining lymph nodes, we first quantified the changes in signal intensity in ROIs localized in the nasal turbinates and the nasopharynx (Fig 4 a,b,c; Supp Fig.4 a,b). Dynamic imaging showed in the group of 12 month old mice, a delayed and significantly reduced transport of contrast agent in these two regions.

At other regions suggested to be efflux sites from the skull, CSF contrast agent signal could be detected in the jugular region below the skull and around the optic nerves (Fig 4 a,d,e; Supp Fig.4 c,d). However, at these two regions, our quantifications revealed that no significant differences in the signal intensity at any time point were observed between the young and 12 month old groups. In fact, the jugular region appeared to show a trend towards increased signal intensity over time in the 12 month old mice compared to the young mice indicating that this region may be a site of accumulation of contrast agent. An earlier report has shown that dural lymphatic vessels of this region become more hyperplastic with age (11).

Thus, as the expected differences in signal dynamics between young and older animals were only detectable in the nasal turbinate and the nasopharyngeal areas, we conclude that this route is one of the major pathways for CSF clearance from the cranium to the cervical lymph nodes.

Histological confirmation of CSF outflow route(s) to the nasopharyngeal lymphatics

Interestingly, the signal quantifications revealed that only a minimal increase of signal (170% in young mice, 85% in 12 month old mice) could be detected within the turbinates themselves in either group, whereas much larger signal increases were detected at the nasopharynx (710% in young mice, 570% in 12 month old mice). This may suggest that the contrast agent distributes to a large area throughout the nasal cavity after effluxing through the cribriform plate before draining to the lymphatic vessels near the nasopharynx leading to the lymph nodes, as appears to be evident from the sagittal view in Video 1.

To further evaluate how CSF tracers drain through the cribriform plate to reach lymphatics surrounding the nasopharynx, we have injected AlexaFluor647-labeled ovalbumin (AF647-OVA) using the same slow infusion protocol employed within the MRI and have assessed the presence of tracer on sections from decalcified craniums and deep cervical lymph nodes. Lymphatic vessels have been identified using LYVE-1 antibodies. As seen in Figure 5a,b taken from two coronal sections at different levels of the nasal cavity, AF647-OVA is clearly associated with olfactory nerves crossing the cribriform plate and is distributed throughout a wide volume of nasal mucosal tissue. A rich network of LYVE1$^+$ lymphatic vessels exists laterally on both sides of the nasopharynx and these vessels could be found containing AF647-OVA signal (Figure 5c-e). Deep cervical lymph nodes located downstream of this site also contained AF647-OVA that was found within LYVE-1$^+$ lymphatic sinuses (Figure 5f-j). Thus, this serves as histological confirmation of the CSF drainage route visible on the MRI.

Discussion

In this study, we have assessed CSF outflow by MRI in two different age groups (2-3 months and 12 months) of mice by utilizing an indwelling catheter system to allow low-rate infusion of a macromolecular contrast agent during a series of image acquisitions. Similar to previous reports, we found slower dynamics of CSF circulation in the older cohort of mice compared to the younger mice. Imaging of the contrast agent dynamics in the cranial region revealed that the bulk of the CSF flowed ventrally under the brain through the basal cisterns and exited through the cribriform plate to be collected by lymphatics in the nasopharyngeal region.

Our methods are similar to those within recent publications utilizing MRI for examination of CSF flow in rodents (11, 12, 15). In these studies, the authors infused contrast agents within the MRI into the cisterna magna through a cannula and examined the efflux routes from the cranial cavity. In our study, we chose to infuse into the ventricles, close to the source of production at the choroid plexuses, which allowed assessment of the clearance from the ventricular system, as well as distribution to and efflux from the subarachnoid space.

We observed minimal contrast agent signal in the dorsal region near the dural sinuses or above the cortical hemispheres. Thus, this is contrary to a concept of a major pathway of CSF outflow at the dorsal dura, as proposed in several recent studies in mice (9, 28, 29) and recently extended to the human situation (37). Instead, the dynamics clearly indicated that the majority of contrast agent traversed the basal cisterns with pathways from the cisterna magna to the subarachnoid space around the circle of Willis. This is consistent with both historical data (1, 38) and other recent MRI studies (8, 11, 12, 15, 24, 33). While it is clear that some portion of CSF does reach the surface of the cortical hemispheres as well as the subarachnoid cisterns located near the dural sinuses (12, 13, 39, 40) the significance and ultimate egress route(s) for this flow remain open questions.

As we anticipated, our data indicates that there is a reduction in CSF outflow in older mice consistent with previous reports (7, 11, 14, 41). We were able to detect delays in 12 month-old animals in CSF clearance and transport at several locations along the CSF flow pathways, including the lateral ventricle, basal cisterns, cervical spinal subarachnoid space, nasal turbinates, nasopharyngeal lymphatics and CNS-draining lymph nodes. Thus, the data is indicative of an overall reduction in CSF turnover with aging. The reason for this diminished turnover of CSF is not yet clear, however, it may be related to a reduced CSF production by the choroid plexuses (27, 42), morphological changes in the dural lymphatics (11) or a reduced transport within lymphatic vessels outside the CNS (43-45). Whether this slowed CSF circulation plays a role in the development of neurodegenerative disorders associated with aging, as speculated in many recent studies (11, 46), remained to be determined.

We took advantage of the differences in contrast agent dynamics between the two different age groups of mice to attempt to elucidate the relative importance of several potential efflux routes. We hypothesized that only along the major bulk flow pathways for CSF egress would the patterns of contrast agent dynamics between the two age groups mirror those seen at the downstream lymph nodes. Since we found that limited contrast agent signal was apparent along the dorsal aspect of the skull, we focused these efforts on potential efflux routes from the basal cisterns. From this location, evidence exists in the literature for outflow to the lymphatic system through the cribriform plate (1, 5, 7, 16, 17, 19, 47), along the sheaths surrounding the optic nerves (7, 48, 49), through the jugular foramina (7, 10, 11, 15, 47) and from the spinal column (13, 23, 50). Of these routes, in our study only the spinal and nasal regions appeared to exhibit the expected contrast enhancement dynamics between the two age groups of mice. An outflow pathway to the lymphatic system does indeed exist in rodents from the sacral region of the spine, however, our previous work and others have determined that under normal conditions the spinal pathways are minor compared to the cranial efflux routes (13, 51, 52). Thus, the resulting conclusion of a major CSF outflow pathway through the cribriform plate would be in agreement with many previous studies (14, 18, 53, 54). Strong supporting evidence for this conclusion comes from experiments blocking this pathway which resulted in dramatic decreases in tracer recovery outside the CNS and increased intracranial pressure during fluid challenge (53, 55). However, we cannot rule out at this point that more direct pathways may exist from the basal skull to reach the nasopharyngeal lymphatics.

This conclusion appears to conflict with that of Ahn et al. in rats who determined using MRI imaging with a macromolecular constrast agent that basal meningeal lymphatic vessels draining through the jugular foramina are the major route for CSF macromolecular uptake and drainage. It must be noted that in their study Ahn et al. did not investigate any potential efflux through the cribriform plate region. However, another possible explanation for this discrepancy may be due to different experimental conditions between our study and Ahn et al. In a recent elegant MRI study by Stanton et al, the authors have demonstrated that the choice of anesthesia has a significant effect on the amount of efflux through the cribriform plate, with mice under isoflurane anesthesia demonstrating much less Gd-DTPA signal in this area (15). This study is consistent with earlier work demonstrating differences in CSF flow dynamics under different types of anaesthesia (8, 13, 56). The authors demonstrated that mice under 1.5% anesthesia exhibited more signal at the jugular foramina along the cranial nerves and also to the spinal canal, indicating that shunting of the CSF flow may occur under certain conditions (15). This potential redirection of flow is an important factor to consider, especially in the context of pathological conditions such as hydrocephalus or glioblastoma, which may block CSF outflow pathways at the skull and reroute flow to the spine (57, 58).

The situation in humans remains unresolved (6). Studies have presented evidence both for and against efflux of contrast agent through the cribriform plate (54, 59-61). One recent clinical MRI study has concluded that CSF efflux to the nasal region is minimal in humans

(61). This paper used a low molecular weight gadolinium contrast agent injected into the lumbar intrathecal space and examined the nasal turbinates at multiple timepoints in patients with various CSF disorders. Although contrast agent was observable in almost half the patients below the cribriform plate along the olfactory nerves, the authors were unable to observe a significant increase of signal within the nasal cavity at any time point. Our current study demonstrates the technical difficulty of detecting significant contrast agent signal enhancement within nasal tissue using an MRI approach, even though we employed a macromolecular contrast agent that should be expected to clear exclusively from the nasal submucosa through lymphatics (53). While the exact anatomical routes remain to be elucidated, it is evident from our decalcified sections after ovalbumin infusion that the contrast agent spreads throughout a wide volume of the nasal tissue after crossing the cribriform plate, which may partially account for the difficulty in detecting signal with MRI in humans.

In sum, through establishment of a technique allowing dynamic CE-MRI under low-rate infusion of gadolinium contrast agents, we conclude that CSF distributes from the ventricles to the subarachnoid space ventral to the brain and in a caudal direction down the spine. Under our experimental conditions, a significant outflow route from the cranium appeared to be through the nasal region to reach lymphatic vessels near the nasopharynx before draining to the cervical lymph nodes. With aging, the dynamics of clearance from the ventricles and flow through the nasal tubinates and nasopharyngeal lymphatics to the lymph nodes were reduced. These experiments have set the stage for further MRI evaluation of CSF outflow in mouse models of neurological disorders.

Methods

Mice

Female wild-type mice (Janvier, France) on the C57BL/6 background were kept under specific pathogen-free conditions until they were used for experimental studies.

Surgical preparation

Mice were anesthetized by intraperitoneal injection of 100 mg/kg ketamine and 20 mg/kg xylazine and fixed in a stereotaxic frame (Kopf Instruments, Tujunga, CA). Under this narcosis, the skull was thinned with a Proxxon GG 12 Engraving drill (Proxxon, Niersbach, Germany). A 28G, 2.5-mm-long MRI-compatible microcannula (#328OP/PK/Spc; Plastics One) was inserted stereotactically 0.95 mm lateral and 0.22 mm caudal to the bregma and 2.50 mm ventral to the skull surface (13). The microcannula was sealed with cyanoacrylate glue. Animals were transferred into the magnet in a prone position on an MRI cradle (BioSpec Avance III 94/20; Bruker Biospin GmbH, Ettlingen, Germany). A 1-1.5m long polyethylene catheter filled with a Gadospin D (nanoPET Pharma GmbH, Germany) solution at a Gd concentration of 25 mM was connected to the MRI compatible

435 microcannula and a 10-μl syringe operated by an MRI compatible NanoJet syringe pump
436 (Chemyx Inc., Stafford, TX, USA). The skin incision was then closed with a medical
437 adhesive bandage around the cannula and the catheter. Animals were allowed to breathe
438 spontaneously during the entire experimental procedure. Respiratory rate and
439 temperature were measured with non-invasive probes (SA Instruments, Stony Brook,
440 NY). Throughout the experiment, the body temperature was maintained between 36.5°C
441 and 37.5°C. During the course of the MRI measurement, the initial narcotic was
442 supplemented as necessary with 0.5-1% isoflurane delivered in 98% O_2 to keep the
443 breathing rate lower than 140 breaths per min.

444 Dynamic contrast-enhanced MRI of the head-neck

445 Animals were examined in a horizontal-bore 9.4 T animal scanner (BioSpec Avance III
446 94/20; Bruker Biospin GmbH, Ettlingen, Germany) with a BGA12S gradient system with
447 ParaVision 6.0.1 (Bruker Biospin GmbH) and a linearly polarized coil with an inner
448 diameter of 40 mm (Bruker Biospin GmbH). Contrast-enhanced imaging was achieved
449 with a three-dimensional time of flight gradient recalled echo sequence (3D-TOF-GRE)
450 originally adapted for imaging of peripheral lymph vessels (62) with a recovery time of
451 12.0 ms, echo time = 2.5 ms, flip angle = 25°, a matrix of 600 × 432 × 180, field of view
452 36.00 mm × 25.92 mm × 18.00 mm, 1 average and a scan time of 4 min 19 s 200 ms. A
453 phantom placed in the vicinity of the animal's head (solution diluted in 0.9% NaCl at 5 mM
454 gadolinium) was used for image intensity normalization over the time series. Following a
455 pre-contrast scan, a Gadospin D solution at 25 mM Gd was infused at a constant rate of
456 0.1 µl/min for 60 min. Total scan time was between 95 and 99 min.
457

458 Data processing

459 ROIs were manually drawn around the different anatomical regions investigated with
460 Horos (version 3.3.6, Horos Project). Signal intensity was normalized using the reference
461 phantom. The normalized ROI value (provided in the supplemental data) was calculated
462 by dividing the original ROI value by the phantom value of the same scan. Contrast agent
463 efflux over time was determined by calculating the percentage change of signal intensity
464 as a function of time after infusion of the contrast agent using the following equation:
465 [(normalized signal intensity – normalized pre-contrast intensity)/ (normalized pre-
466 contrast intensity)] × 100. Ventricle and lymph node volumes were quantified using semi-
467 automatic segmentation tools in 3DSlicer, version 4.11 (www.slicer.org). All the digital
468 imaging and communications in medicine images were imported into 3D Slicer for the
469 segmentation and 3D modelling. The region of interest was first defined and segmented
470 with the segment editor module. The model maker module was used to create the 3D
471 model. Finally, the volume was determined via the segment statistics module.
472

473 Histological analysis of tracer efflux to lymphatics

For experiments where ventricular infusions were followed by histological analysis an identical procedure was used with the following modifications: a solution of ovalbumin-Alexa647 (Thermo Fisher Scientific, Waltham, MA, USA) dissolved in artificial CSF (Harvard Apparatus, Holliston, MA, USA) at a concentration of 5 mg/mL was infused at a constant rate of 0.1 µL/min for 60 min; the 2-3 months wild-type mice were sacrificed at the end of the infusion.

For decalcification, intracardiac perfusion with PBS and 4% PFA was performed. Afterwards, the mice were decapitated followed by the removal of skin, muscles, incisors and lower jaw from the cranium. The cranium was then immersed in 4% PFA for overnight fixation before being placed in 14% EDTA for 7 days (refreshed daily) at 4°C. Decalcified tissue was then immersed in 30% sucrose for 3 days for cryoprotection before OCT embedding. 20µm-thick coronal sections were cut from a cryostat (Cryostar NX50) and stored at -80°C. For immunofluorescence staining of LYVE-1, frozen tissues were first hydrated with PBS for 10 minutes, then permeabilized by 0.1% triton for 10 minutes. 10% goat serum was used for blocking for 1 hour at room temperature. Tissues were incubated with primary antibody (rabbit anti-Lyve-1, AngioBio, catalogue 11-034, 1:600 dilution) for 3 hours at room temperature and then washed with PBS before incubating with secondary antibody (goat anti-rabbit Alexa488) for 2 hours at room temperature. Imaging of the nasal region was done under Zeiss Axiozoom V16 microscope equipped with a Photometrics PrimeBSI sCMOS camera combined with a LED illumination system pe-4000 and ZEN 2 software (Carl Zeiss). Higher magnification images were then acquired using a Zeiss LSM800 confocal microscope.

For processing of draining lymph nodes, cervical lymph nodes were post-fixed in 4% PFA at 4 °C overnight. Lymph nodes were further immersed in 30% sucrose for 2 days at 4 °C before being snap-frozen in melting isopentane with liquid nitrogen. The frozen tissue was cut serially into 15 μm sections with a cryostat microtome (Leica Microsystems, Wetzlar, Germany). Sections were incubated with an anti-LYVE-1 (eBioscience, San Diego,CA, USA, clone ALY7, 1:200) primary antibody for 2 hours at room temperature before incubation with a Donkey anti-rat (Invitrogen, Grand Island, NY, 1:1000) secondary antibody conjugated with Alexa488 for 1 hour at room temperature. Sections were finally counterstained with DAPI. Regions of interest were acquired with a Zeiss LSM 880 Axio Observer.

Statistics

Statistical analyses were performed with GraphPad Prism 5 (GraphPad). Graphs represent mean ± SEM. Means of two groups were compared using an unpaired two-tailed Student's t test. Two-way ANOVAs were used for comparison with time points being a within-subject factor and age being a between-subject factor, followed by Bonferroni's posthoc test. A p-value <0.05 was considered statistically significant.

Study approval

All mouse experiments were approved by the Landesamt für Gesundheit und Verbraucherschutz, Saarbruecken, Germany (license numbers 31/2018 and 45/2019).

Author contributions

Y.D. and S.T.P. conceived and designed the study. Y.D. performed the MRI experiments. Y.D., L.X. and A.S. performed the histology experiments. J.K., Y.D and S.T.P. analyzed the data. A.M. and Y.D. applied for approval of animal experiments. A.M. maintained the MRI facility. K.F. made substantial contributions to the conception of the study. Y.D. and S.T.P drafted the manuscript. All authors have approved the final version of the manuscript and have agreed to be accountable for all aspects of the work.

Acknowledgements

We also thank Prof. Walter J. Schulz-Schaeffer for his critical reading of the manuscript. The authors also thank Prof. Arno Bücker and Prof. Michael D. Menger for their support of the MRI facility. This work was supported by the Medical Faculty of the University of the Saarland (HOMFOR 2019) to Y.D. and a Swiss National Science Foundation grant (310030_189226) to S.T.P. The authors declare no competing financial interests.

References

1. Weed LH. Studies on cerebro-spinal fluid. No. IV : The dual source of cerebro-spinal fluid. *J Med Res.* 1914;31(1):93-118 11.
2. Davson H, and Segal MB. *Physiology of the CSF and blood-brain barriers.* Boca Raton etc.: CRC Press; 1996.
3. Bradbury MWB, and Cserr HF. In: Johnston MG ed. *Experimental biology of the lymphatic circulation*. Amsterdam: Elsevier; 1985:355-94.
4. McComb JG. Recent research into the nature of cerebrospinal fluid formation and absorption. *J Neurosurg.* 1983;59(3):369-83.
5. Koh L, et al. Integration of the subarachnoid space and lymphatics: is it time to embrace a new concept of cerebrospinal fluid absorption? *Cerebrospinal Fluid Res.* 2005;2:6.
6. Proulx ST. Cerebrospinal fluid outflow: a review of the historical and contemporary evidence for arachnoid villi, perineural routes, and dural lymphatics. *Cell Mol Life Sci.* 2021.
7. Ma Q, et al. Outflow of cerebrospinal fluid is predominantly through lymphatic vessels and is reduced in aged mice. *Nat Commun.* 2017;8(1):1434.
8. Ma Q, et al. Rapid lymphatic efflux limits cerebrospinal fluid flow to the brain. *Acta Neuropathol.* 2019;137(1):151-65.

9. Louveau A, et al. Structural and functional features of central nervous system lymphatic vessels. *Nature.* 2015;523(7560):337-41.
10. Aspelund A, et al. A dural lymphatic vascular system that drains brain interstitial fluid and macromolecules. *J Exp Med.* 2015;212(7):991-9.
11. Ahn JH, et al. Meningeal lymphatic vessels at the skull base drain cerebrospinal fluid. *Nature.* 2019;572:62-6.
12. Pizzo ME, et al. Intrathecal antibody distribution in the rat brain: surface diffusion, perivascular transport and osmotic enhancement of delivery. *J Physiol.* 2018;596(3):445-75.
13. Ma Q, et al. Clearance of cerebrospinal fluid from the sacral spine through lymphatic vessels. *J Exp Med.* 2019;216(11):2492-502.
14. Brady M, et al. Cerebrospinal fluid drainage kinetics across the cribriform plate are reduced with aging. *Fluids Barriers CNS.* 2020;17(1):71.
15. Stanton EH, et al. Mapping of CSF transport using high spatiotemporal resolution dynamic contrast-enhanced MRI in mice: Effect of anesthesia. *Magn Reson Med.* 2021.
16. Faber WM. The nasal mucosa and the subarachnoid space. *Am J Anat.* 1937;62(1):121-48.
17. Erlich SS, et al. Ultrastructural morphology of the olfactory pathway for cerebrospinal fluid drainage in the rabbit. *J Neurosurg.* 1986;64(3):466-73.
18. Kida S, et al. CSF drains directly from the subarachnoid space into nasal lymphatics in the rat. Anatomy, histology and immunological significance. *Neuropathol Appl Neurobiol.* 1993;19(6):480-8.
19. Norwood JN, et al. Anatomical basis and physiological role of cerebrospinal fluid transport through the murine cribriform plate. *eLife.* 2019;8:1-32.
20. Hsu M, et al. Neuroinflammation-induced lymphangiogenesis near the cribriform plate contributes to drainage of CNS-derived antigens and immune cells. *Nat Commun.* 2019;10(1):229.
21. Mortensen AO, and Sullivan WE. The cerebrospinal fluid and the cervical lymph nodes. *Anat Rec.* 1933;56(4):359-63.
22. Pile-Spellman JM, et al. Experimental in vivo imaging of the cranial perineural lymphatic pathway. *AJNR Am J Neuroradiol.* 1984;5(5):539-45.
23. Kwon S, et al. Fluorescence imaging of lymphatic outflow of cerebrospinal fluid in mice. *J Immunol Methods.* 2017;449:37-43.
24. Yamada S, et al. MRI tracer study of the cerebrospinal fluid drainage pathway in normal and hydrocephalic guinea pig brain. *Tokai J Exp Clin Med.* 2005;30(1):21-9.
25. Hladky SB, and Barrand MA. Mechanisms of fluid movement into, through and out of the brain: evaluation of the evidence. *Fluids Barriers CNS.* 2014;11(1):26.
26. Steffensen AB, et al. Cotransporter-mediated water transport underlying cerebrospinal fluid formation. *Nat Commun.* 2018;9(1):2167.
27. Liu G, et al. Direct Measurement of Cerebrospinal Fluid Production in Mice. *Cell Rep.* 2020;33(12):108524.

28. Louveau A, et al. CNS lymphatic drainage and neuroinflammation are regulated by meningeal lymphatic vasculature. *Nat Neurosci.* 2018;21(10):1380-91.
29. Rustenhoven J, et al. Functional characterization of the dural sinuses as a neuroimmune interface. *Cell.* 2021.
30. Oliver G, et al. The Lymphatic Vasculature in the 21(st) Century: Novel Functional Roles in Homeostasis and Disease. *Cell.* 2020;182(2):270-96.
31. Iliff JJ, et al. Brain-wide pathway for waste clearance captured by contrast-enhanced MRI. *J Clin Invest.* 2013;123(3):1299-309.
32. Lee H, et al. The Effect of Body Posture on Brain Glymphatic Transport. *J Neurosci.* 2015;35(31):11034-44.
33. Gakuba C, et al. General anesthesia inhibits the activity of the “glymphatic system". *Theranostics.* 2018;8(3):710-22.
34. Gaberel T, et al. Impaired glymphatic perfusion after strokes revealed by contrast-enhanced MRI: a new target for fibrinolysis? *Stroke.* 2014;45(10):3092-6.
35. Ringstad G, et al. Brain-wide glymphatic enhancement and clearance in humans assessed with MRI. *JCI Insight.* 2018;3(13).
36. Xue Y, et al. In vivo T1 mapping for quantifying glymphatic system transport and cervical lymph node drainage. *Sci Rep.* 2020;10(1):14592.
37. Ringstad G, and Eide PK. Cerebrospinal fluid tracer efflux to parasagittal dura in humans. *Nat Commun.* 2020;11(1):354.
38. Ghersi-Egea JF, et al. Rapid distribution of intraventricularly administered sucrose into cerebrospinal fluid cisterns via subarachnoid velae in rat. *Neuroscience.* 1996;75(4):1271-88.
39. Mestre H, et al. Flow of cerebrospinal fluid is driven by arterial pulsations and is reduced in hypertension. *Nat Commun.* 2018;9(1):4878.
40. Bedussi B, et al. Paravascular spaces at the brain surface: Low resistance pathways for cerebrospinal fluid flow. *J Cereb Blood Flow Metab.* 2018;38(4):719-26.
41. Nagra G, and Johnston MG. Impact of ageing on lymphatic cerebrospinal fluid absorption in the rat. *Neuropathol Appl Neurobiol.* 2007;33(6):684-91.
42. Preston JE. Ageing choroid plexus-cerebrospinal fluid system. *Microsc Res Tech.* 2001;52(1):31-7.
43. Karaman S, et al. Decline of lymphatic vessel density and function in murine skin during aging. *Angiogenesis.* 2015;18(4):489-98.
44. Proulx ST, et al. Quantitative measurement of lymphatic function in mice by noninvasive near-infrared imaging of a peripheral vein. *JCI Insight.* 2017;2(1):e90861.
45. Zolla V, et al. Aging-related anatomical and biochemical changes in lymphatic collectors impair lymph transport, fluid homeostasis, and pathogen clearance. *Aging Cell.* 2015;14(4):582-94.
46. Da Mesquita S, et al. Functional aspects of meningeal lymphatics in ageing and Alzheimer's disease. *Nature.* 2018;560(7717):185-91.

47. Schwalbe G. Die Arachnoidalraum ein Lymphraum und sein Zusammenhang mit den Perichorioidalraum. [The arachnoidal space as a lymphatic space with connection to the perichoroidal compartment.]. *Zbl med Wiss* 1869;7:465–7.
48. Erlich SS, et al. Ultrastructure of the orbital pathway for cerebrospinal fluid drainage in rabbits. *J Neurosurg.* 1989;70(6):926-31.
49. Ludemann W, et al. Ultrastructure of the cerebrospinal fluid outflow along the optic nerve into the lymphatic system. *Child Nerv Syst.* 2005;21(2):96-103.
50. Brierley JB, and Field EJ. The connexions of the spinal sub-arachnoid space with the lymphatic system. *J Anat.* 1948;82(3):153-66.
51. Marmarou A, et al. Compartmental analysis of compliance and outflow resistance of the cerebrospinal fluid system. *J Neurosurg.* 1975;43:523-34.
52. Bozanovic-Sosic R, et al. Spinal and cranial contributions to total cerebrospinal fluid transport. *Am J Physiol-Reg I.* 2001;281(3):R909-R16.
53. Bradbury MW, and Westrop RJ. Factors influencing exit of substances from cerebrospinal fluid into deep cervical lymph of the rabbit. *J Physiol.* 1983;339:519-34.
54. Johnston M, et al. Evidence of connections between cerebrospinal fluid and nasal lymphatic vessels in humans, non-human primates and other mammalian species. *Cerebrospinal Fluid Res.* 2004;1(1):2.
55. Mollanji R, et al. Intracranial pressure accommodation is impaired by blocking pathways leading to extracranial lymphatics. *Am J Physiol Regul Integr Comp Physiol.* 2001;280(5):R1573-81.
56. Hablitz LM, et al. Increased glymphatic influx is correlated with high EEG delta power and low heart rate in mice under anesthesia. *Sci Adv.* 2019;5(2):eaav5447.
57. Voelz K, et al. A ferritin tracer study of compensatory spinal CSF outflow pathways in kaolin-induced hydrocephalus. *Acta Neuropathol.* 2007;113(5):569-75.
58. Ma Q, et al. Lymphatic outflow of cerebrospinal fluid is reduced in glioma. *Sci Rep.* 2019;9(1):14815.
59. Lowhagen P, et al. The Nasal Route of Cerebrospinal-Fluid Drainage in Man - a Light-Microscope Study. *Neuropathol Appl Neurobiol.* 1994;20(6):543-50.
60. de Leon MJ, et al. Cerebrospinal Fluid Clearance in Alzheimer Disease Measured with Dynamic PET. *J Nucl Med.* 2017;58(9):1471-6.
61. Melin E, et al. In vivo assessment of cerebrospinal fluid efflux to nasal mucosa in humans. *Sci Rep.* 2020;10(1):14974.
62. Muller A, et al. Magnetic resonance lymphography at 9.4 T using a Gadolinium-based nanoparticle in rats. Investigations in healthy animals and in a hindlimb lymphedema model. *Invest Radiol.* 2017;52(12):725-33.

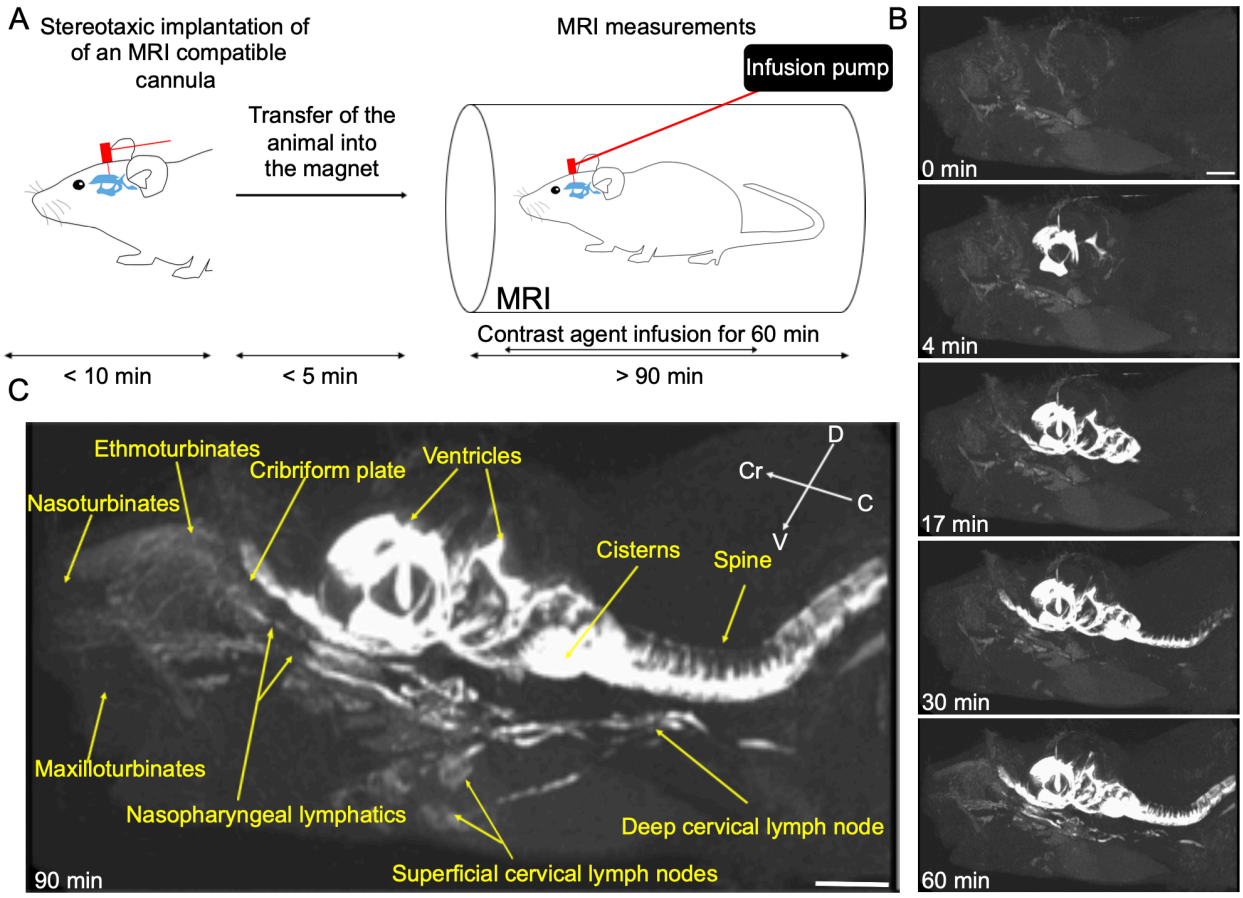

Figure 1: Dynamic CE-MRI shows continuous efflux of contrast agent from the nasal region through lymphatic vessels to cervical lymph nodes following low-rate ventricular infusion. A Schematic representation of the experimental setup. MRI-compatible cannulae were stereotactically implanted into the ventricle of 2-3 months old C57BL/6J mice anesthetized with ketamine/xylazine. The animals were then transferred into a horizontal-bore 9.4 T MRI. Polyethylene tubing containing the contrast agent (Gadospin D solution at 25 mM Gd) was attached connecting the cannula and the infusion pump. Before tracer infusion, T1-weighted (3D time-of-flight gradient recalled echo sequence) MRI measurements were started and followed by intraventricular low-rate infusion (0.1 µl/min) of the tracer while MRI acquisitions continued. **B** Representative signal dynamics using maximum-intensity projections visualizing the entire head-neck region. Following the beginning of contrast agent infusion, enhancement of the signal intensity in the ventricle is detectable at 4 min, in the nasal cavity at 17 min, and in the neck lymph nodes at 30 and 60 min. **C** Visualization of the spread of tracer after 90 min demonstrating continuous signal enhancement from the cribriform plate to the nasopharyngeal lymphatic vessels to cervical lymph nodes. Data are representative of n = 7 mice and three independent experiments. Scale bars: 3 mm.

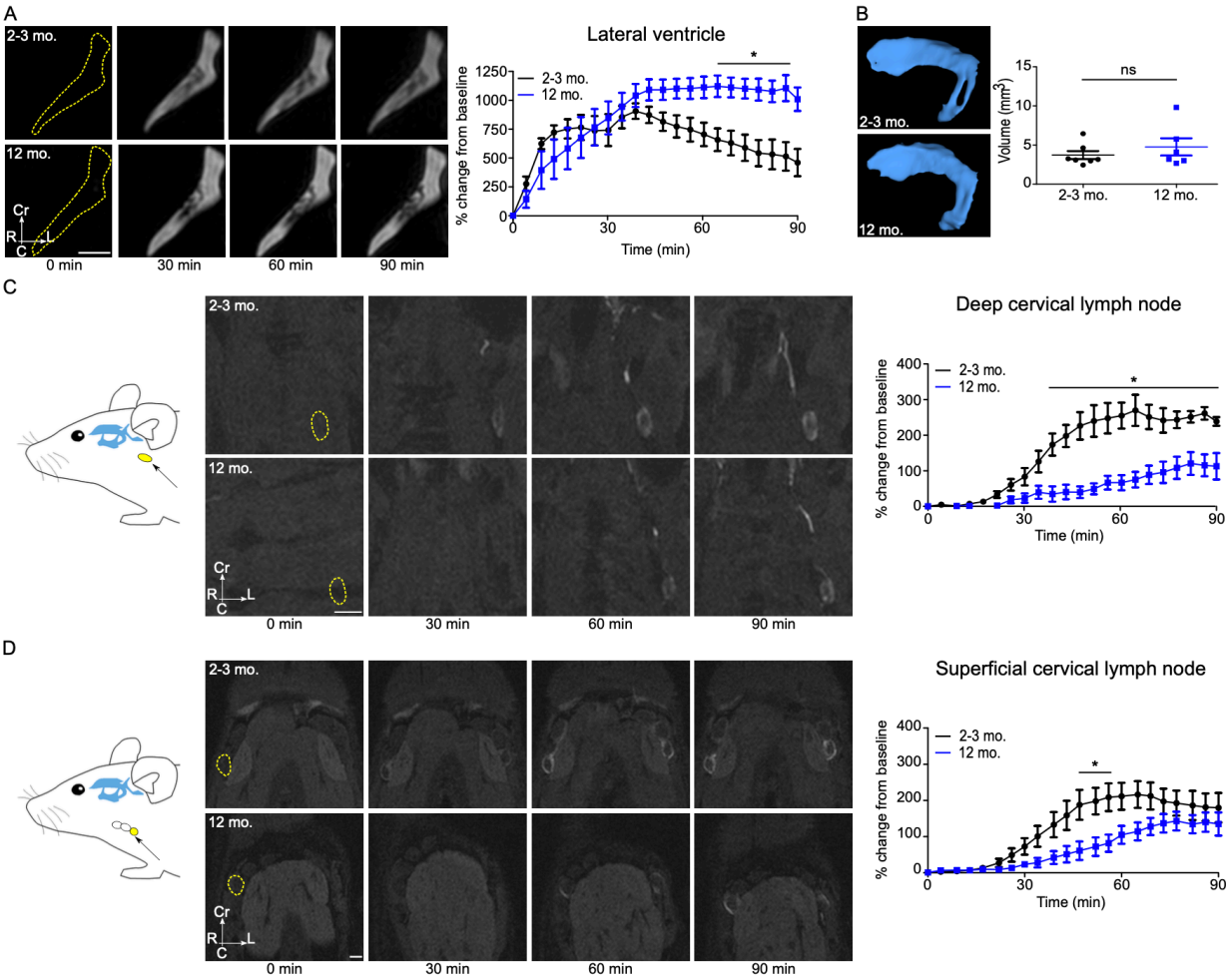

Figure 2: Clearance from ventricles and efflux to lymph nodes are reduced in 12 months old mice. Visualization of tracer spread after low-rate intraventricular infusion (0.1 µl/min) of a Gadospin D solution at 25 mM; data acquired with a series of T1-weighted MRI measurements (3D time-of-flight gradient recalled echo sequence). **A** Signal dynamics of Gadospin D contrast agent showing clearance from the contralateral-ventricles in the horizontal plane in 2-3 months and 12 months old mice. **B** Representative images of 3D reconstruction of the contralateral-ventricles of 2-3 months and 12 months old mice. Ventricle volumes of 2-3 months and 12 months old mice were compared with two-tailed Student's t-test. **C-D** Signal dynamics in the horizontal plane of Gadospin D tracer efflux to deep and superficial cervical lymph nodes in 2-3 months and 12 months old mice. ROIs shown in yellow. Data are expressed as mean ± SEM of n= 7 2-3 months old mice vs n=6 12 months old mice and are representative of three independent experiments.. *p<0.05 (two-way ANOVA followed by Bonferroni's posthoc test). Scale bars: 1 mm.

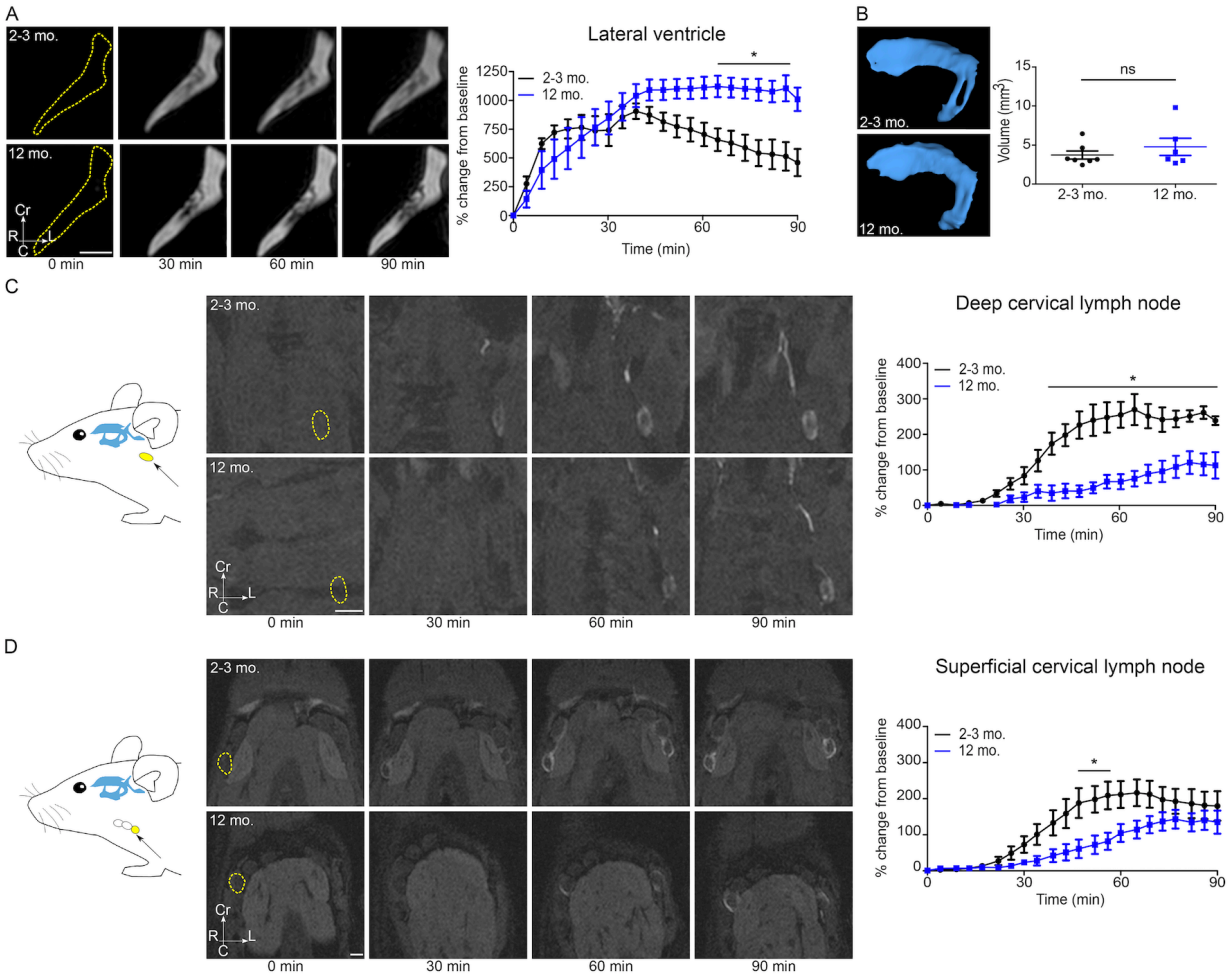

Figure 3: CSF predominantly clears along the ventral aspect of the skull. Visualization of tracer clearance after low-rate intraventricular infusion (0.1 µl/min) of Gadospin D solution at 25 mM Gd. Data were acquired with a series of T1-weighted MRI measurements (3D time-of-flight gradient recalled echo sequence). **A** Overview scheme of ROI location. **B,C** Coronal sections demonstrating in 2-3 months and 12 months old mice the dynamics of CSF efflux in representative ROIs (shown in yellow) of the dorsal aspect of the skull: in the perisagittal superior sinus and the quadrigeminal cisterns. **D,E** Horizontal sections showing the dynamic of CSF efflux in the ventral aspect of the skull in 2-3 months and 12 months old mice: around the circle of Willis and around the internal carotid (ROIs in yellow). Quantifications of the different ROIs are expressed as the mean ± SEM of n= 7 2-3 months old mice vs n=6 12 months old mice and are representative of three independent experiments. *p<0.05, (two-way ANOVA followed by Bonferroni's posthoc test). Scale bars: 1 mm.

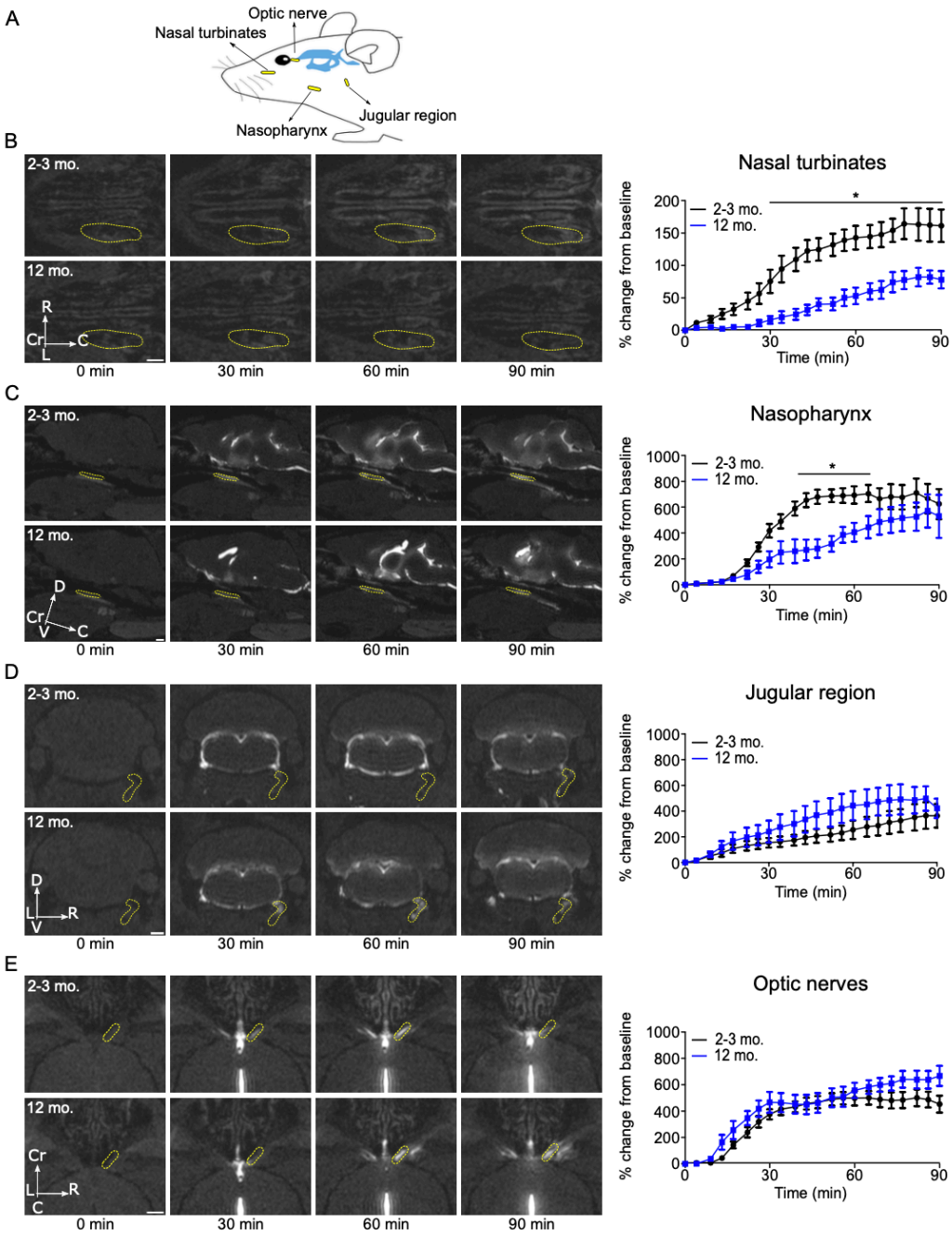

Figure 4: Clearance of CSF from the cranium is reduced with aging in the nasal turbinates and the nasopharynx but not in the jugular region and around the optic nerves. Imaging of tracer clearance after low-rate intraventricular infusion (0.1 µl/min) of Gadospin D solution at 25 mM Gd. Data were acquired with a series of T1-weighted MRI measurements (3D time-of-flight gradient recalled echo sequence). **A** Overview scheme of ROI location. **B** Horizontal sections demonstrating the dynamics of CSF efflux to nasal turbinates in 2-3 months and 12 months old mice. **C** Sagittal sections reveal the dynamics of contrast agent in the nasopharynx in the two groups of mice. **D** Coronal sections demonstrating the CSF efflux from the jugular region in the groups of mice of different ages. **E** Horizontal sections showing CSF efflux along the optic nerve in 2-3 months and 12 months old mice. Quantifications of the different ROIs (shown in yellow) are expressed as the mean ± SEM of n= 7 2-3 months old mice vs n=6 12 months old mice and are representative of three independent experiments. *p<0.05 (two-way ANOVA followed by Bonferroni's posthoc test). Scale bars: 1 mm.

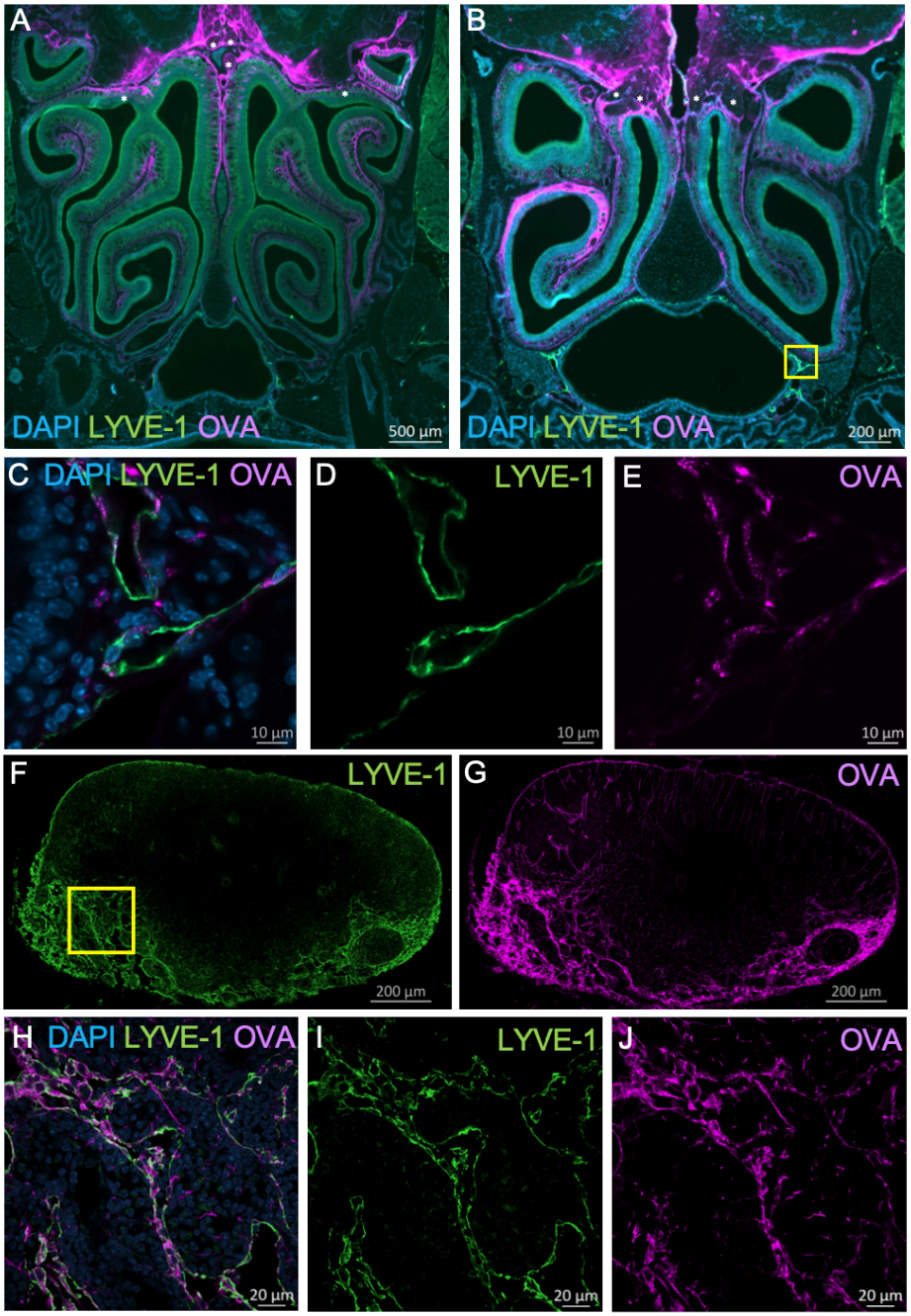

Figure 5: Histological validation of CSF tracer efflux through the cribriform plate to nasopharyngeal lymphatics and to deep cervical lymph nodes. Fluorescently-labeled ovalbumin (OVA) was introduced via low-rate intraventricular infusion (0.1 µl/min for 60 min) and at 90 min the mice were sacrificed for post-mortem analysis of tracer efflux. **A, B** Coronal sections of decalcified skulls demonstrating significant efflux of OVA into the nasal mucosal tissues. OVA (purple) can be seen crossing the cribriform plate alongside several olfactory nerve bundles (indicated with *). Lymphatic vessels (stained with LYVE-1 in green) can be found in proximity to the nasopharynx under the nasal turbinates. **C-E** High-magnification view of the nasopharyngeal region indicated by the yellow box in B, demonstrating OVA signal within the LYVE-1$^+$ lymphatic vessels. **F, G** Sections of deep cervical lymph nodes indicating close association of OVA signal within lymphatic sinuses stained with LYVE-1. **H-J** High-magnification view of the region indicated by the yellow box in F, demonstrating OVA signal within the LYVE-1$^+$ lymphatic sinuses. Data are representative of n = 6 mice and two independent experiments.